Materials & Design 228 (2023) 111855

Contents lists available at ScienceDirect

Materials & Design

journal homepage: www.elsevier.com/locate/matdes

Controlling the cell and surface architecture of cellulose nanofiber/PVA/$Ti_3C_2T_X$ MXene hybrid cryogels for optimized permittivity and EMI shielding performance

Riikka Haataja [a], Sami Myllymäki [b], Ossi Laitinen [a], Heli Jantunen [b], Henrikki Liimatainen [a,*]

[a] Fibre and Particle Engineering, P.O. Box 4300, FI-90014, University of Oulu, Oulu, Finland
[b] Microelectronics Research Unit, P.O. Box 4500, FI-90014, University of Oulu, Oulu, Finland

HIGHLIGHTS

- Aligned $Ti_3C_2T_x$/CNF/PVA hybrid cryogels were prepared by freeze-drying.
- Cell and surface structure of cryogels was manipulated by simple adjustments to freezing process.
- The GHz and THz signal permittivity of cryogels was dominated by their surface structure.
- The combination of designed bulk and surface layer could compensate even 20 wt % higher filler contents.
- The produced green cryogels proved to be efficient in EMI shielding.

GRAPHICAL ABSTRACT

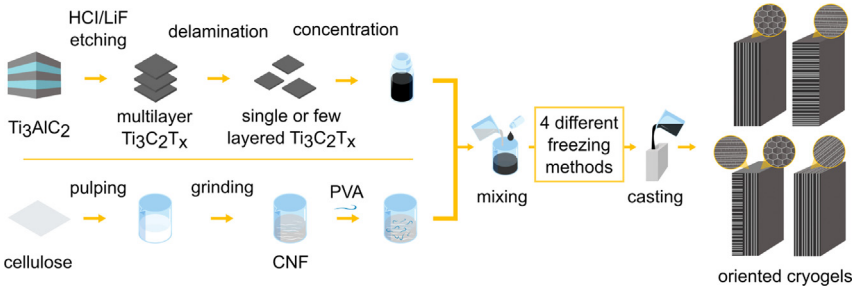

ARTICLE INFO

Article history:
Received 24 January 2023
Revised 17 March 2023
Accepted 21 March 2023
Available online 24 March 2023

Keywords:
Aerogel
Composite
Electromagnetic interference shielding
Green electronics
Nanocellulose

ABSTRACT

Anisotropic, nanoporous structures are promising materials for manipulating the propagation of electromagnetic waves at millimeter and sub-THz frequencies as well as for electromagnetic interference (EMI) shielding with rapidly evolving green electronics. In this work, cell and surface architecture of sustainable hybrid cryogels of cellulose nanofibers, polyvinyl alcohol (PVA) and $Ti_3C_2T_X$ MXene was controlled to adjust their GHz and THz dielectric permittivity and EMI shielding performance. Temperature gradient freeze-drying was used to obtain aligned honeycomb and lamellar pore structures with specific surface layer designs. The millimeter wave permittivity varied relative to thickness direction as the side of cryogels that was directly exposed to cold gradient had systematically a higher permittivity. This anisotropy was caused by a thin, smooth outermost surface layer covering the open core structure. The surface designs of all cryogels dominated signal permittivity, and the effects of higher MXene dosages could be offset by the surface layer. Cryogels with dense surface layer containing 70 and 50 wt % of MXene displayed very high average attenuation levels of 52.1 and 37.2 dB, respectively. Overall, the results show that the structural design of porous hybrid material can be used to adjust their EMI shielding performance at GHz and THz frequencies.

© 2023 The Author(s). Published by Elsevier Ltd. This is an open access article under the CC BY-NC-ND license (http://creativecommons.org/licenses/by-nc-nd/4.0/).

1. Introduction

Electromagnetic interference (EMI) is a growing concern [1–4] with rapidly advancing electronic systems and equipment used e.g., in telecommunication [5], health care and biomedicine [6],

* Corresponding author.
E-mail address: Henrikki.liimatainen@oulu.fi (H. Liimatainen).

https://doi.org/10.1016/j.matdes.2023.111855
0264-1275/© 2023 The Author(s). Published by Elsevier Ltd.
This is an open access article under the CC BY-NC-ND license (http://creativecommons.org/licenses/by-nc-nd/4.0/).

and military [7]. All electric devices and components, such as emerging wearable and portable electronics, emit electromagnetic waves that, if not adequately shielded, can interfere with neighboring component, the actual device, other electronic devices, or users [3,4]. The ubiquitous consumer electronics have augmented the EMI difficulties causing telecommunication signal interference resulting in slower data rates and connection problems [8]. Therefore, the device must be protected from interfering signals scattered everywhere in modern society. EMI shielding materials attenuate electromagnetic waves by reflection and absorption, with absorption often being the preferred mechanism. Particularly advantageous is that EMI absorbers can eliminate secondary electromagnetic pollution by preventing secondary reflections, which is critical e.g., in stealth applications [9–11].

Light-weight porous structures are attractive designs for EMI shielding as the large solid-air interface area promotes reflection and absorption of electromagnetic radiation [12–14]. Besides bulk porous solids relying on synthetic materials such as polyurethane [15–17], melamine [18–20] or polystyrene [21–23], nanoporous aero- and cryogels made from biopolymers using supercritical or freeze-drying processes offer sustainable alternatives to fabricate high-performance EMI shields [24–27]. Especially, elongated and flexible nano-entities derived from cellulose, that is, cellulose nanofibers (CNF), can be used as a skeleton for mechanically robust nanofoams [28–31]. The three-dimensional (3D) interconnected network of CNF can be incorporated with conductive fillers, such as silver nanowires [32,33], carbon nanotubes [34,35], or graphene [36,37], to produce environmentally friendly and durable EMI shielding materials needed for sustainable electronics manufacturing. Recently, MXenes, 2D transition metal carbides, especially $Ti_3C_2T_X$, have shown excellent electrical properties for future EMI shielding designs [4,17,38,39]. MXenes have a general formula of $M_{n+1}X_nT_X$, where M is a transition metal, *X* is carbon or nitrogen, and T_X represents a surface termination. [40–42].

Anisotropic structures are promising for EMI shielding purposes, particularly as their reflection and attenuation features can be adjusted by the cell orientation relative to impinging electromagnetic waves [43]. In addition to typical randomly oriented or unidirectional honeycomb structures, more complex pore cell architecture such as bi- or multidirectional orientation or lamellar cell walls connected via CNF bridges [44,45] can be manufactured by using more than one temperature gradient. These structures have already shown promising results in EMI shielding in composites based on graphene [46] and MXene [47,48]. Different layered designs can also be used to manipulate the propagation of EM-waves [49–51]. Controlled 3D structures can have a remarkable effect on material performance [49–51] and can help to obtain an improved EMI shielding properties. Previously only a few green cryogel hybrids of nanocellulose and MXene with isotropic or anisotropic structures have been revealed [43,52,53] and to the best of our knowledge the effect of surface structure of cryogels on attenuation of electromagnetic waves is unexplored. In this study, the role of cell architecture of cross-linked hybrid cryogels of cellulose nanofibers, polyvinyl alcohol (PVA), and Ti3C2T_X MXene in millimeter wave permittivity and EMI shielding performance was elucidated. Based on oriented temperature gradient freezing, honeycomb and lamellar cryogels were designed with different surface architectures to achieve higher attenuation levels with as little material as possible. By adjusting only the freezing method, both the bulk and surface structure could be controlled to form efficient EMI shielding cryogels from sustainable raw materials. Simulations and experiments were used to characterize material loss and permittivity at millimeter and sub-THz frequencies.

2. Experimental section

2.1. Materials

Cellulose nanofibers were prepared using a mechanical grinding method adopted from Laitinen et al. (2020) [54]. First, 100 g (abs.) birch cellulose pulp from UPM (Finland) was soaked with 2000 g of deionized water overnight. Then, using a wet disintegrator at 30,000 rpm, three parallel pulp batches were wet disintegrated in accordance with ISO 5263-1:2004. Next, 100 g of disintegrated pulp with a consistency of 1.5 wt % was ground using a Masuko supermasscolloider (MKCA6-2J, Japan). The pulp was passed through the grinder 14 times using the following grinding stone gap values: 0 μm for three times, −20 μm for three times, −40 μm for three times, −60 μm for three times, −80 μm once, and −90 μm once. Finally, 1.7 wt % nanocellulose suspension was collected and stored at 4 °C.

Ti_3AlC_2 MAX phase (400 mesh) was obtained from 11Technology (China). PVA (87 %–89 % hydrolyzed, MW 85,000–124,000) and LiF (99.995 %) were ordered from Sigma-Aldrich (Finland). HCl 37 % (analytical grade) was purchased from VWR Merck (Finland).

2.2. Preparation of MXene ink

$Ti_3C_2T_X$ MXene nanoflake ink was prepared by the method proposed by Alhabeb et al. [12]. First, 30 ml of 9 M HCl was added to a PTFE bottle and 2.4 g of LiF was carefully mixed in small portions with HCl with continuous stirring. The bottle was then placed in an ice bath, and 1.5 g of MAX phase was added gradually. The mixture was continuously stirred and left to react for 24 h at room temperature. The entire synthesis process was conducted in a fume hood to eliminate possible *in-situ* formed HF gases. After 24 h, the mixture was pipetted into four 50 ml centrifuge tubes, which were then filled with deionized water and centrifuged at 1900 G for 5 min. The supernatant was carefully decanted, and the residual MXene sludge was re-dispersed in two centrifuge tubes, each filled with 40 ml of deionized water, and the washing process was repeated until the pH of the supernatant was ~ 6. The bottles were vigorously hand-shaken for 15 min and then centrifuged at 1900 G for 1 h. Finally, the obtained single (or few) layered MXene ink was collected and stored in closed glass vials at 4 °C. The synthesis was repeated five times, after which the MXene inks were combined and concentrated with a vacuum rotary evaporator to prepare aqueous inks with concentrations up to 27.3 mg/ml.

2.3. Preparation of aligned hybrid cryogels

The cross-linked and conductive hybrid cryogels of CNF, PVA, and MXene ink were fabricated by first mixing 1.7 wt % CNF hydrogel with 4.0 wt % PVA solution in a weight ratio of 3:4 and diluting the solution to 8 mg/ml with deionized water. The cross-linking reaction between CNF and PVA was allowed to react under continuous stirring for 2 h at room temperature. Then, concentrated MXene ink was bath sonicated for 2 min before dosing (70 wt %, 50 wt %, 30 wt %, and 10 wt %) to the CNF–PVA mixture, after which the solution was further stirred for 2 h. The mixture was poured into 50 × 50 × 3 mm PTFE molds and frozen on a copper plate placed in liquid nitrogen. The anisotropic cell structure of the cryogels was controlled by placing the mold on a copper plate in different positions (Fig. 1a). First, the mold was placed vertically, i.e., with its 3 × 50 mm side (side 4) against the cold finger, resulting in a unidirectional A-type sample. B-type samples were frozen unidirectionally with their 50 × 50 mm side (side 3) facing the copper plate. C-type samples with two directional layers were created

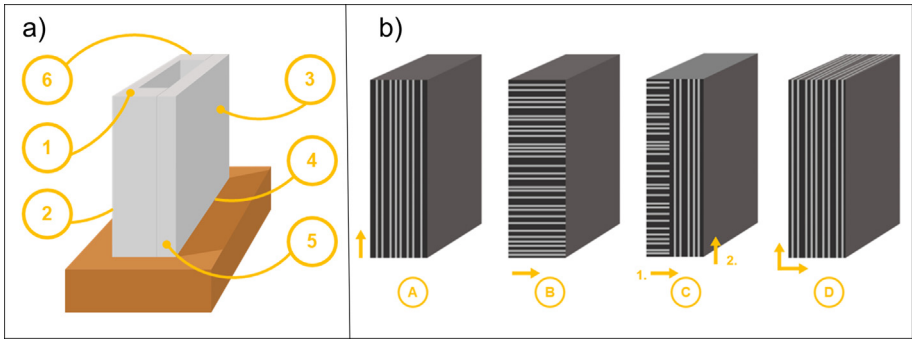

Fig. 1. (a) Geometry of a freezing mold, (b) oriented hybrid cryogels with honeycomb (a and b), two-layer honeycomb (c), and lamellar structure (d).

using first horizontal freezing direction (side 3) and then turning the mold when the freezing was halfway to stand on side 4. D-type samples were frozen with side 3 against the cold finger, so the mold was influenced by two cold gradients, one from the cold finger and another from evaporating nitrogen around the mold. After the directional freezing, the samples were freeze-dried at − 54 °C using a Scanvac Coolsafe freeze-dryer (55–15 Pro, Denmark) with a vacuum pressure of ~ 0.01 mbar for 36 h. The hybrid cryogels were named according to the freezing method (A, B, C, and D) and MXene wt % (10, 30, 50, and 70). A 100 % MXene cryogel was fabricated as a reference.

2.4. Characterizations

XRD measurements for drop-casted MXene films were made with a Rigaku SmartLab 4.5 kW (Japan) with a Co source (40 kV and 135 mA) Cu K-β at a scan rate of 4° min^{-1}, scan angle 2θ of 5°–80° and a step of 0.02°. X-ray photoelectron spectroscopy (XPS) analysis was conducted using the Thermo Fisher Scientific ESCALAB 250Xi XPS System (UK). MXene ink was drop-casted on a Si plate and measured with a K-α source with passage energies of 150 eV for a survey and 20 eV for high-resolution spectra. The surface layer of the cryogels was scratched off for analysis, and the measurement was conducted similarly. Field emission scanning electron microscopy (FESEM) (JEOL JSM-7900F, Japan) was used to characterize the morphology and cell structure of the platinum-coated cryogel samples with an acceleration voltage of 5 kV. FESEM images were taken from cutting angles perpendicular and parallel to the cold finger (cutting angles 1&2 in Fig. S6c). Transmission electron microscopy (TEM) images and energy-dispersive X-ray spectroscopy (EDS) data were obtained using TEM (JEOL JEM-2200FS, Japan) with an acceleration voltage of 200 kV. A laser diffraction spectrometer (Malvern Zetasizer Nano, UK) was used to measure flake size distribution and zeta potential of MXene ink. Cryogels' physical dimensions were used to calculate their densities and porosities (Table S1). Zwick/Roell universal testing machine (Germany) was used to measure the compressive strength of aerogels.

2.5. Permittivity and EMI shielding measurements

Millimeter wave material characterization and conductivity measurements were performed with the reflection signal measurements (DAK3.5-TL-P: 200 MHz–20 GHz by Speag corporation, Switzerland), transmission/reflection signal measurements with WR-42 waveguides (18–26.5 GHz by Keysight corporation, USA), and the THz characterization with Terapulse 4000 (60 GHz–2.5 THz, Teraview corporation, UK). The measurements were conducted from both sides of the specimens. Scattering parameters from vector network analyzer from DAK and waveguide measurements were calculated either as permittivity or loss values. DAK measurements present the material characteristics in terms of the measurement probe's physical location at 3 mm wide spot with the reflected circular polarized signal. Waveguide measurements show the material characteristics of a 10 × 4 mm sample with the transmitted linear polarized signal, while Terapulse measurements depict material characteristics of a 12 mm-diameter disc using a transmitted linear polarized signal. Thus, DAK indicated the permittivity characteristics on the surface position without signal vector orientation, whereas waveguide and Terapulse measurements presented permittivity characteristics through the material sample with the signal vector orientation related to the material's structural orientations, as shown in Fig. 2. Material permittivity was calculated using commercial software form Speag, Keysight, and Teraview. Permittivity formulas [56] and material parameters were simulated with CST Studio Suite 2021.

3. Results and discussion

Aligned and cross-linked hybrid cryogels of cellulose nanofibers, PVA, and $Ti_3C_2T_X$ MXene were designed by controlling the cell architecture during the freeze-drying process. Temperature gradient freezing resulted in hierarchical and highly porous structures with unidirectional honeycomb (A- and B-type samples), two-layered honeycomb (C-type samples), or lamellar (D-type samples) pore architectures (Fig. 1). The conductivity of the cryogels was adjusted by incorporating colloidal one- or few-layered $Ti_3C_2T_X$ MXene ink, which was synthesized by etching the Al layer from the Ti_3AlC_2 MAX phase. After that, experiments and simulations were used to elucidate the role of anisotropic pore alignment of cryogels in permittivity, loss characterization, and EMI shielding properties at millimeter and sub-THz frequencies.

3.1. MXene ink

MXene ink was exfoliated using MILD-method [55] in which the Ti_3AlC_2 MAX phase is first etched to remove the Al layer, and the synthesized $Ti_3C_2T_X$ MXene multilayered flakes are further delaminated by intercalation of Li^+ ions originating from LiF. The synthesized MXene ink had a greenish color, a distinct feature of colloidal $Ti_3C_2T_X$ dispersion [57]. The MXene ink also exhibited a Tyndall effect (Fig. S1a and b), indicating the formation of a stable colloidal dispersion of $Ti_3C_2T_X$ flakes. [58] FESEM images (Fig. 3a and b) of the MAX phase before and after the etching and delamination treatment corroborated that the MAX phase was effectively converted into MXene flakes. The presence of single and few-layered $Ti_3C_2T_X$ flakes was confirmed by TEM (average single-flake thickness of 0.9 nm, Fig. 3c, and S1c) and their hexagonal structure by diffractogram (Fig. S1d). The XRD analysis of the MAX phase and drop-casted MXene film (Fig. S2) showed that the 002 peaks of

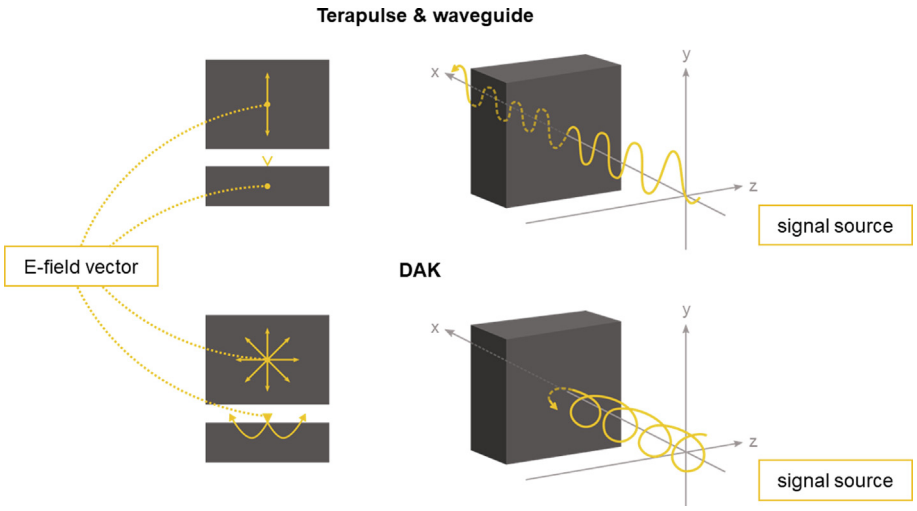

Fig. 2. Electric field vectors and propagation characteristics used in material characterization performed with DAK, waveguide, and Terapulse devices. Electric field vectors on sample surfaces are presented on the left, and corresponding wave propagation is illustrated on the right.

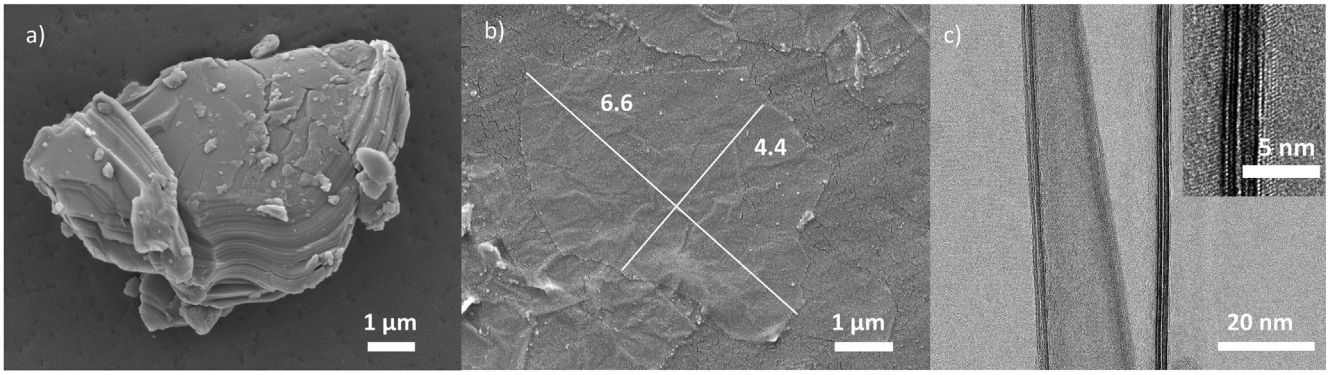

Fig. 3. FESEM images of (a) MAX phase and (b) a few-layered MXene flake on paper substrate, and (c) TEM image of two-layered MXene flakes on a carbon grid with insert of a close-up of flake layers.

MXene were shifted to lower 2θ angles (centered at 8.22°) because of enlargened d-spacing caused by the removal of Al layer [55,57]. Additionally, the delaminated flakes reassembled into a film-aligned in-plane, which caused domination of 00 L peaks in the spectra. The peak broadening indicated a decrease in the crystalline size of MXenes compared to MAX phase powder. Drop-casted MXene films were also analyzed with XPS (Fig. S3), which displayed that Al peaks disappeared [57]. EDS analysis further confirmed this phenomenon (Fig. S4, Table S1). According to size distribution analysis (Fig. S5), MXene flakes had a median lateral diameter of 5.7 µm.

3.2. Structure of aligned hybrid cryogels

All the CNF/PVA/MXene hybrid formulations formed self-standing and flexible porous nanofoams having a dark appearance caused by the MXene (Fig. 4). The PVA reinforced the cryogel structure, and the used PVA dosage was optimized in our earlier study [59]. The samples with 30 wt % or higher MXene content were more durable and had fewer cracks and defects than those with 10 wt % of MXene. Densities of the cryogels (MXene content from 10 to 70 wt %) varied from 9.3 mg/cm^3 to 27.7 mg/cm^3 and porosities from 98.9 % to 99.4 % (Table S2). These ultra-high porosities are comparable to those previously reported [60–63] for pure aerogels and cryogels of nanocelluloses, and show that the MXene was mainly adhered on the CNF surfaces without significantly filling the open pores of the nanofiber network. The hybrid cryogels could be easily bent and were durable when an external force was applied parallel to the freezing direction (Fig. 4). However, the cryogels became stiffer and lost some flexibility with increasing MXene concentration. On the other hand, 10 wt % samples could not resist deformations from mechanical stress so well. The durability and compression strength of a hybrid cryogel having a MXene content of 50 wt % (A50) was displayed by loading the cryogel with a 500 g weight (Fig. 4b) without any visible deformations in cryogel structure. Compression strengths measured with Zwick for A10 and A50 are presented in Fig. S8. The cryogel prepared directly from pure MXene in the absence of a supporting CNF–PVA network was, in turn, very weak and dusty and could not be properly handled. However, the pure MXene cryogel had a very low density of 0.9 mg/cm^3, which caused the formation of a ribbon-like structure (Fig. S6a).

The structure and cell alignment of hybrid cryogels were investigated more closely by FESEM imaging. The A-type samples (Fig. 4d) were remarkably stronger and displayed fewer structural deformations than those prepared with other methods. These cryogels comprised a rather uniform and typical honeycomb structure, the pore channels having unidirectional and vertical (from side 1 to side 4, Fig. 1) alignment. B-type samples had a similar unidirectional structure to A-type cryogels, but the honeycomb cells were oriented horizontally, from side 2 to side 3. C-type cryogels had a two-layered structure consisting of two combined sections of hor-

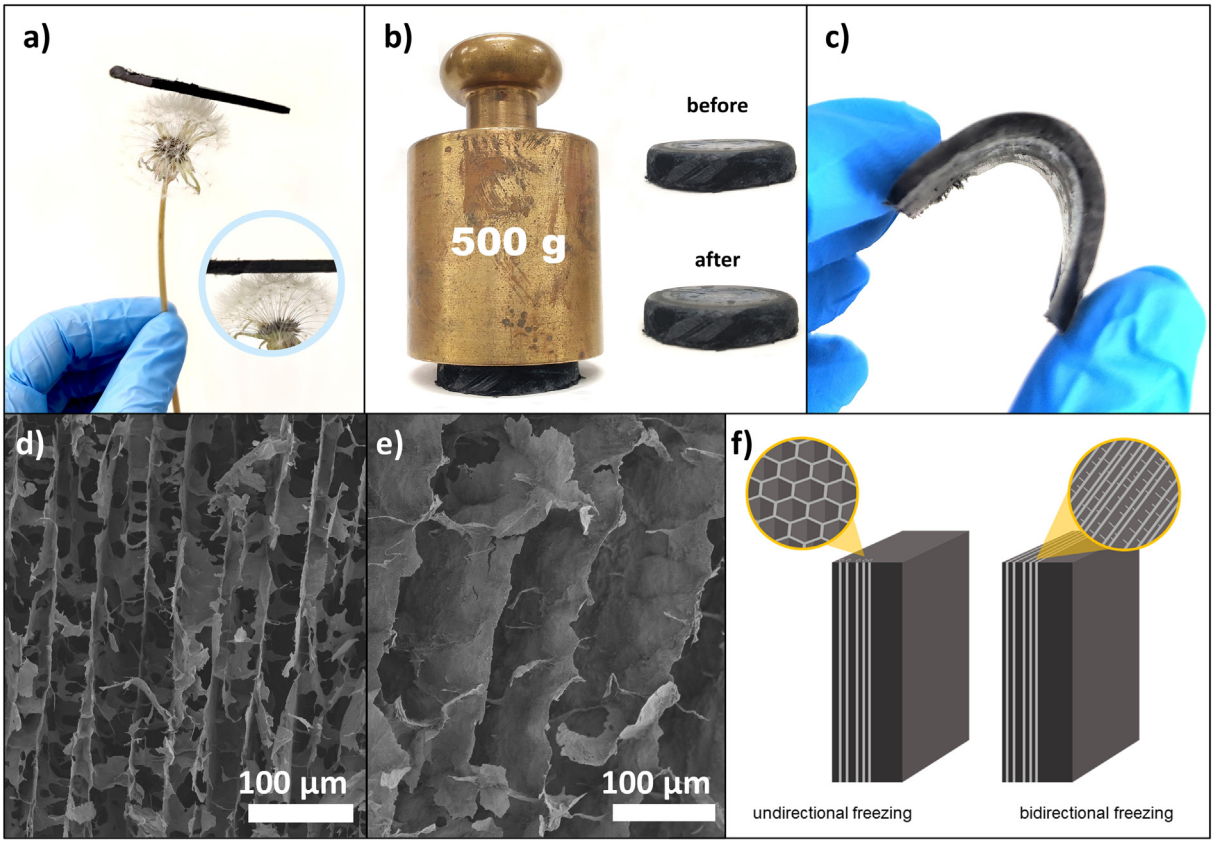

Fig. 4. (a) Hybrid cryogel of cellulose nanofibers, PVA, and $ti_3C_2T_X$ MXene standing on a flower (A50). (b) Cylindrical hybrid cryogel (A50) before and after carrying a 500 g weight. (c) Cryogel (A30) being bent. FESEM images of (d) A-type and (e) D-type cryogels consisting of the honeycomb structure and stacked lamellar sheets, respectively, and (f) Graphical presentation of A and D-type cryogel structures.

izontally and vertically oriented pores (2/3 and 1/3 of the thickness, respectively), which were perpendicular to each other. The cell structure of D-type cryogels resembled uniformly oriented stacked lamellar sheets loosely connected to each other with "bridges" (Fig. 4e). The lamellar structure was obtained using a bidirectional freezing process similar to that presented in previous studies [44,45,64,65]. The bidirectional temperature gradient was formed when the thin mold (3 mm) was placed on the cold finger (the first gradient from side 2 to side 3) and simultaneously, the sample stayed covered with evaporated nitrogen (the second gradient from side 1 to side 4). Unlike the D-type samples, B-type samples were affected by the single gradient from the cold finger. The bidirectional temperature gradient significantly affected the pore size of the cryogels as the average distance of cell walls was roughly 35 µm for A-, B- and C-type samples and 110 µm for D-type samples. Additionally, B-, C-, and D-type samples had a surface layer of around 100–200 µm on the side that faced the cold finger. Near the sample surface, the structure was more random, and below this layer, the pores were remarkably smaller than in the main body of the sample (Fig. S7f). Fig. S7 shows the cross-section profiles of cryogels.

3.3. GHz and THz permittivity of anisotropic cryogels

The electromagnetic interaction between dielectric materials is described by dielectric permittivity (ε_r) and loss factor ($tan\delta$). When an electromagnetic wave interacts with a dielectric material, the internal dipoles of the material are reorganized with the electric field, thus resulting in an additional electric dipole, and the material becomes polarized. The degree of polarization to the applied electric field relative to the vacuum gives the relative dielectric permittivity. The real part of permittivity (ε_r') describes energy stored, whereas the imaginary part (ε_r'') describes the loss of energy as shown in Equation (1):

$$\varepsilon_r(\omega) = \varepsilon_r'(\omega) - \varepsilon_r''(\omega) \quad (1)$$

3.3.1. Permittivity of unidirectional hybrid cryogels (A-type) at 200 MHz–20 GHz

Using reflection signal measurements from a DAK device (from 200 MHz to 20 GHz (Fig. 5)), the permittivity of aligned, anisotropic A-type cryogels was analyzed. The permittivity followed the MXene concentration linearly so that the highest permittivity values were achieved with the highest MXene loading, the MXene increases the charging dipoles in the material (Fig. 5a). Permittivity decreased as expected for all samples when moving to higher frequencies. The relationship between oscillation frequency and the mass inertia is related to the angular frequency (ω), which affects the permittivity. A fast decrease in permittivity was observed, especially with high MXene loadings (A50 and A70) in the frequency range from 200 MHz to 20 GHz, after which a plateau level was reached, the maximum level being 19.7 with A70, 14.5 with A50, 6.3 with A30, and 2.0 with A10 at 20 GHz. Loss tangent values of permittivity increased as a function of MXene dosage similarly to real permittivity values, with the exception that A70 had a lower permittivity. However, due to the low permittivity of the calibration material, the DAK measurements suffered from resonances at 7.5 GHz and 15 GHz, which made it difficult to determine the value of the loss tangent, especially at higher permittivity levels.

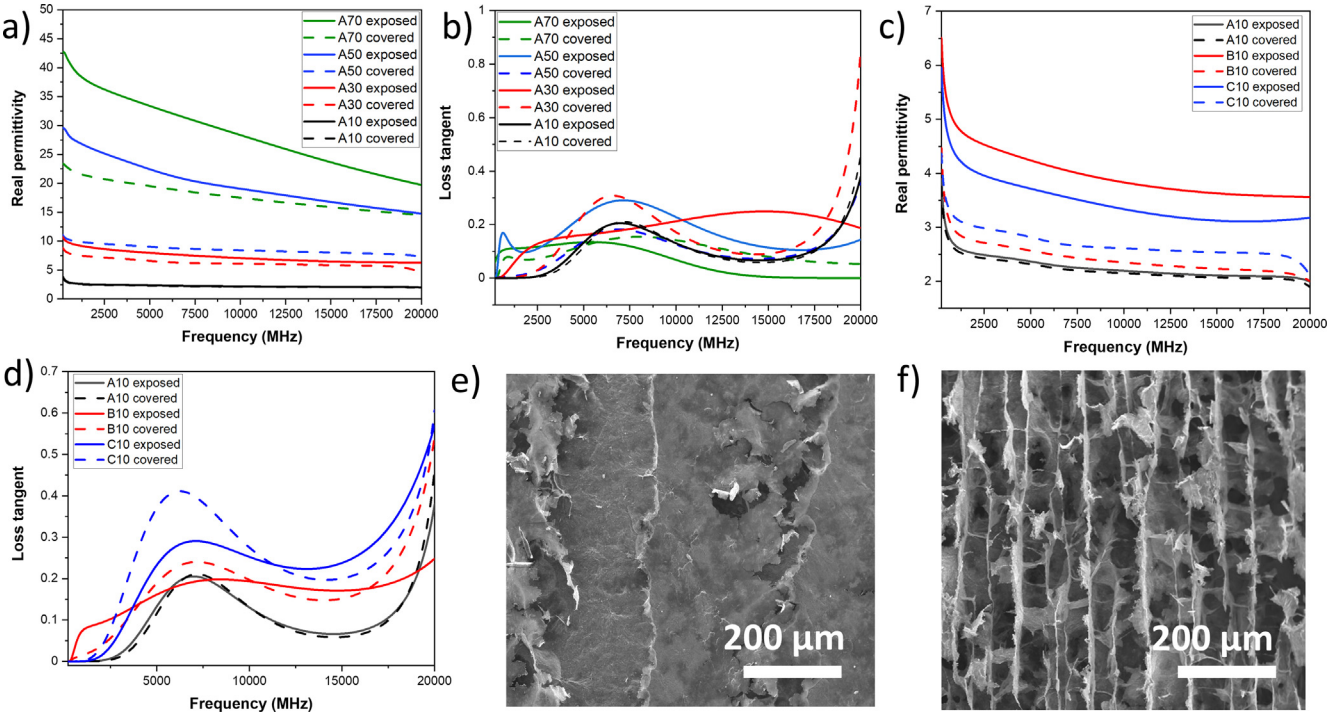

Fig. 5. Permittivity of hybrid unidirectional A-type cryogels from 200 to 2500 MHz. (a) Real part and (b) Loss tangent value (Imaginary part) of permittivity as a function of MXene dosage and surface properties (A10, A30, A50, and A70) (c) Role of cryogel side of samples with same MXene concentration in real permittivity (side exposed to T gradient and opposite side), and (d) loss tangent, and the surface of (e) T exposed side and (f) Opposite side of A70.

Internal cell structure, surface properties, and anisotropic materials' orientation can have a remarkable impact on material dielectric permittivity. Thus, the DAK device was used to measure all samples from both sides with reflected and circular polarized electromagnetic waves. Moreover, each sample was analyzed at five different physical locations, and the average value was calculated. The anisotropy of hybrid cryogels (relative to thickness direction) was clearly noted as the side which was directly exposed to cold gradient had systematically higher permittivity (Fig. 5a, c) and loss tangent (Fig. 5b) compared to the opposite side. For example, A70 had a permittivity of 20 on the exposed side and 15 on the covered side. This phenomenon was presumably due to a difference in surface structure, the side exposed directly to cold gradient having a separate thin and smooth outermost surface layer covering a unidirectional open honeycomb core structure (Fig. 5e). In contrast, this layer was absent on the opposite side (Fig. 5f). Overall, the permittivity values indicated that the smooth surface promoted electromagnetic wave attenuation due to higher permittivity and reflection. Therefore, unless otherwise stated, further analyses were always conducted from the exposed side (having the smooth and thin surface layer, also B-, C-, and D-type samples).

3.3.2. Comparison of GHz and THz permittivities of different cryogel architectures

The role of cell orientation in permittivity at 200–20000 MHz and 100 GHz to 1 THz was examined using A-, B-, and C-type unidirectional and two-layered cryogel designs with a constant MXene content of 10 wt % (Fig. 5c and d). The highest permittivity was observed with a unidirectional structure having the structured honeycomb cells aligning with the signal source (B10). The second-highest permittivity was showed by C10, which consist of two layers of pores oriented parallel and perpendicular toward the signal source. Contrary to these observations, it has previously been observed that a structure with a cell aligned perpendicular to the signal source can attenuate wave front propagation more effectively [43,66]. In this study, the surface structure of cryogels seemed to dominate signal permittivity, while the influence of inner cell structure was not measured separately. This behavior was probably because of the freezing technique, which formed a dense structural surface layer on the side exposed to a temperature gradient. This layer was also created between the pore interfaces of C-type structures (Fig. 6g). The layer improved the attenuation of the wave front significantly, the increase in real permittivity being over 60 % with B10. The surface layer could compensate for the effects of higher MXene dosages. For example, sample A50 from the exposed side had real permittivity of 20.1, whereas, with A70 from the covered side, it was only 18.2 at 8 GHz. Loss tangent values varied only slightly, being the lowest (0.1) for A10, and B10 and C10 having similar values (0.15). The unidirectional honeycomb structure was also compared to a bidirectionally frozen lamellar D-type sample. The bidirectional structure continuously had a higher permittivity than the A-type cryogel with a honeycomb structure. At 8 GHz, the real permittivity of D50 was 23.8, whereas, for A50, it was 20.1. This result was presumably caused by the denser surface structure of D-type sample perpendicular to impinging electromagnetic waves throughout the sample, which promoted the permittivity and resulted in a higher permittivity than the A-type sample (Fig. 5d). In addition, the lamellar structure itself likely increased the permittivity [67]. Same trends were also observed in conductivity measurements, whose results are presented in Table S3.

During the DAK analysis, a circular polarized "U" shaped electric field was created at the end of the probe (Fig. 2). The cell wall position related to electromagnetic waves differed from the waveguide or Terapulse analyses with a vertical electric field because the electric field does not pass the sample but turns back after penetrating the sample surface. A vector of an electromagnetic wave parallel to sample surface dominates in the DAK measurement. Therefore, B- and C-type samples with cell walls oriented perpendicular to the electromagnetic field notably affected wave propagation. The A-

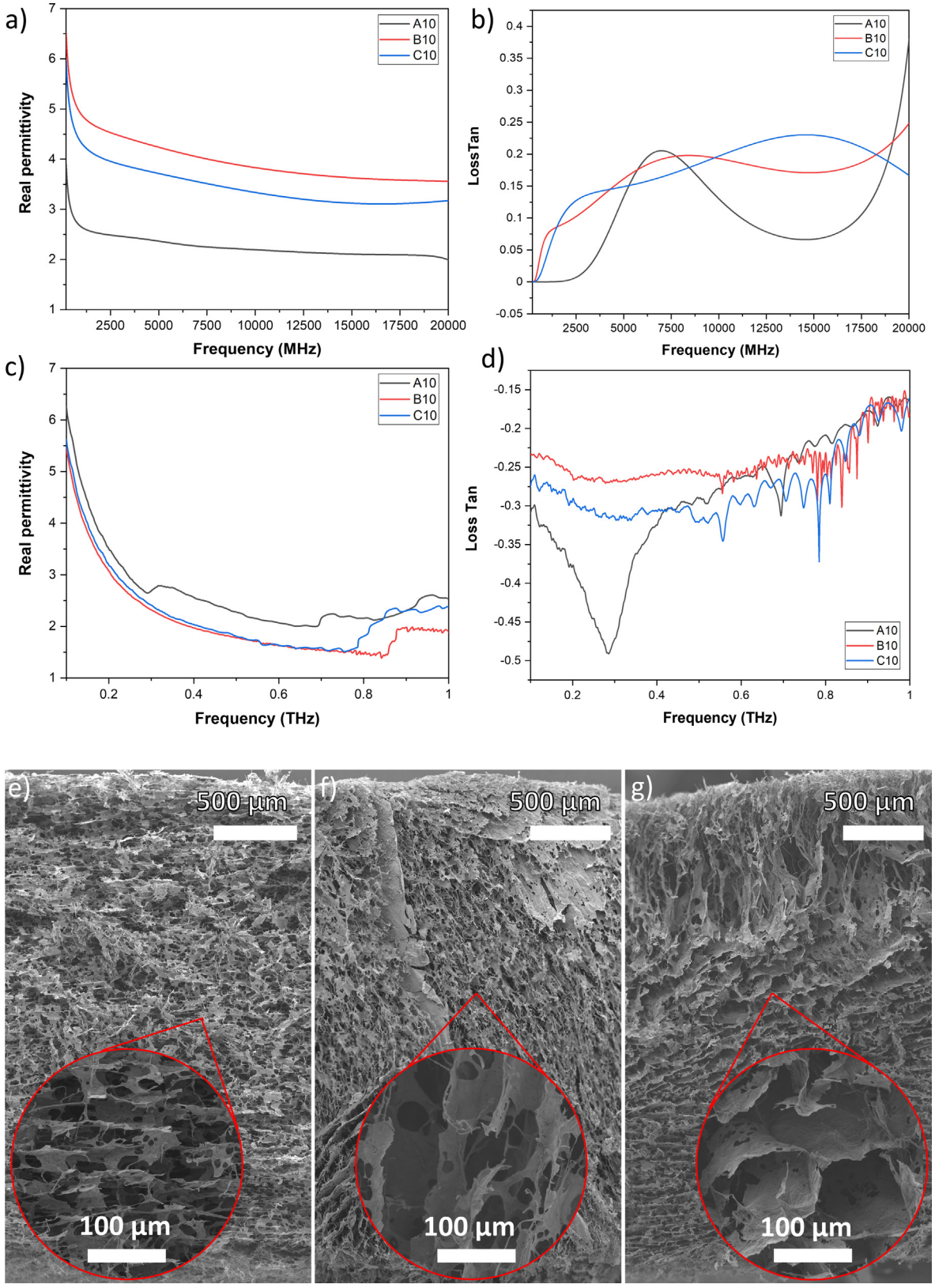

Fig. 6. (a) Real permittivity and (b) Loss tangent from 200 to 20,000 MHz (c) Real permittivity and (d) Loss tangent from 0.1 to 1 THz for A10, B10 and C10 (e) Cross-section of (f) A10, (e) B10, and (g) C10.

type sample had instead open structured honeycomb cells in this direction, allowing wave propagation with lower interactions with the material.

Using the Terapulse device, the permittivity of hybrid cryogels containing 10 wt % of MXene was also displayed at higher frequencies from 0.1 to 1 THz. Higher MXene concentrations completely

blocked the waves, making it impossible to measure them. The measured permittivity of all samples was between 5 and 6 at 0.1 THz and decreased to 2 or below at 1 THz, while loss tangent values were between 0.2 and 0.3. However, the original signal power decreased significantly in these measurements because of the high thickness of the samples, and the permittivity calculation might suffer for inaccuracies.

3.4. EMI shielding efficiency of cryogels from 200 MHz to 20 GHz

EMI shielding performance of materials is often evaluated in terms of application-specific parameters, that is, EMI shielding efficiency (SE). SE describes the attenuation of an electromagnetic wave as a ratio of measured energy or intensity of signal before and after passing the shielding material in decibel units [3]. Total shielding efficiency (SE_T) composes of reflection, absorption, and internal reflections, of which the latter can be neglected when using multilayered shielding materials, such as MXenes, and higher EMI SE values since the internally reflected waves are absorbed by the material when its thickness exceeds the skin depth or SE_A > 10 dB [9,68]. Absorption is often the preferred shielding mechanism because reflection may cause secondary signal pollution to the surrounding environment [69–72].

In many commercial applications, 20 dB is considered a sufficient attenuation level [3,73], meaning that 99 % of incoming energy is blocked. Shielding efficiency from reflection (SE_R) for absorber materials should be less than 3 dB to enable the absorption to dominate [74]. The shielding efficiencies were measured from the unidirectional honeycomb, two-layer honeycomb, and lamellar cryogel designs from 200 to 20,000 MHz. Here, the commercial guideline of 20 dB was easily achieved with samples with 70 and 50 wt % MXene. The highest SE value was achieved with the highest MXene concentration, with A70 at 52.1 dB at 20 GHz (Fig. 7a). The SE decreased with decreasing MXene concentration resulting in 37.2, 17.8, and 6.4 dB for A50, A30, and A10, respectively. The results followed the trends observed in permittivity measurements for different cryogel structures. SE_T at 20 GHz for B10 and C10 were 8.4 and 12.3, whereas A10 achieved only 6.4 dB. Similar to permittivity, the dense surface structures in B-, C-, and D-type samples seemed to improve the shielding performance and be the dominating factor for the EMI shielding performance. The total attenuation increased as the frequency increased because the attenuation constant is proportional to the material's frequency and permittivity values of the material [75].

The role of cryogel structure in shielding performance was demonstrated in terms of SE_T, SE_R, and SE_A and is presented in Fig. 7b and c and at 12 GHz in Table 1. For the highest MXene concentration, SE_A was 49.2 dB, while SE_R remained at 2.3 dB at 20 GHz. For samples A10, B10, and C10, the SE_R was 0.3, 0.5, and 0.8 dB at 20 GHz, respectively. Absorption was observed to be overall higher as SE_A for B10 and C10 were 8.4 and 12.3, whereas A10 achieved only 6.4 dB at 20 GHz, which underlines the importance of surface properties over the inner structure. In addition to the surface structure, the lamellar structure in D-type samples improved the attenuation performance even further. D50 sample achieved SE of 45.8 dB at 20 GHz, whereas A50 remained at 37.2 dB. Fig. 7c illustrates that the reflection remained below 3 dB (on average 2.1 and 2.8 dB at 2–20 GHz for A50 and D50, respectively) even with the higher MXene concentrations and dense surface layer.

Table 1
Shielding efficiency parameters for cryogels at 12 GHz.

Sample	SE_A	SE_R	SE_T
A10	2.5	0.4	2.9
B10	3.5	0.6	4.1
C10	6.0	1.0	7.0
A30	8.8	1.2	10.0
A50	21.8	2.1	23.9
D50	28.8	2.8	31.6
A70	33.7	2.8	36.5

3.5. Simulated permittivities of A-type cryogels at 18–26 GHz

Real permittivity and tangent loss of cryogels were first measured with the WR-42 waveguide setup and then the setup and material were modeled with microwave simulator software. Material permittivity parameters were extracted from the simulation model and are presented in Fig. 8a. Samples A70 and A50 displayed similar real permittivity at a remarkably higher level (25–35) compared to A30 and A10 (5–10). A similar trend was observed with loss tangent values in Fig. 8b. However, the loss tangent values of DAK results (Fig. 5) were significantly lower than the simulated values (0.2–0.3 range vs. 0.4–1.3 range, respectively), indicating that the waveguide method provides more realistic values for material loss tangent. Waveguide-measured and simulated permittivity values were also higher than earlier measured values with the DAK method. In addition, samples were compared with waveguide measurements by turning the orientation from side 2 to side 5, which is not normally used (Fig. S9). Their absorption properties were systematically worse than measured in the original direction, and the difference was noticeable, especially in the case of high MXene concentration.

Corresponding wave propagation and electric field created by the waveguide was simulated and presented as a heat map of signal amplitude in Fig. 8c. The wave is at first propagating in air, and then it squeezes inside the high permittivity material as presented in Fig. 8c–f. In samples B10 and A30 the wavelength is larger than

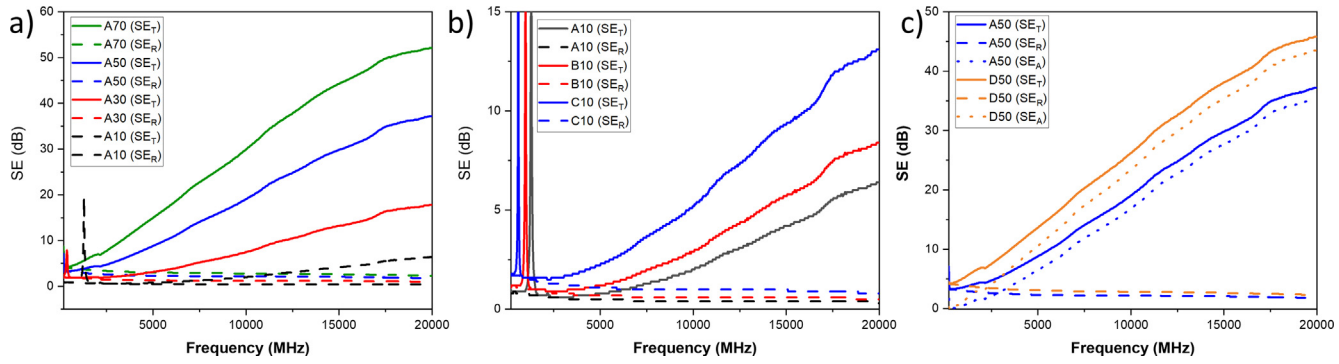

Fig. 7. (a) SE_T values for A-type samples, (b) SE_T and SE_R for A10, B10, and C10, (c) SE_T, SE_R, and SE_A for A50 and D50.

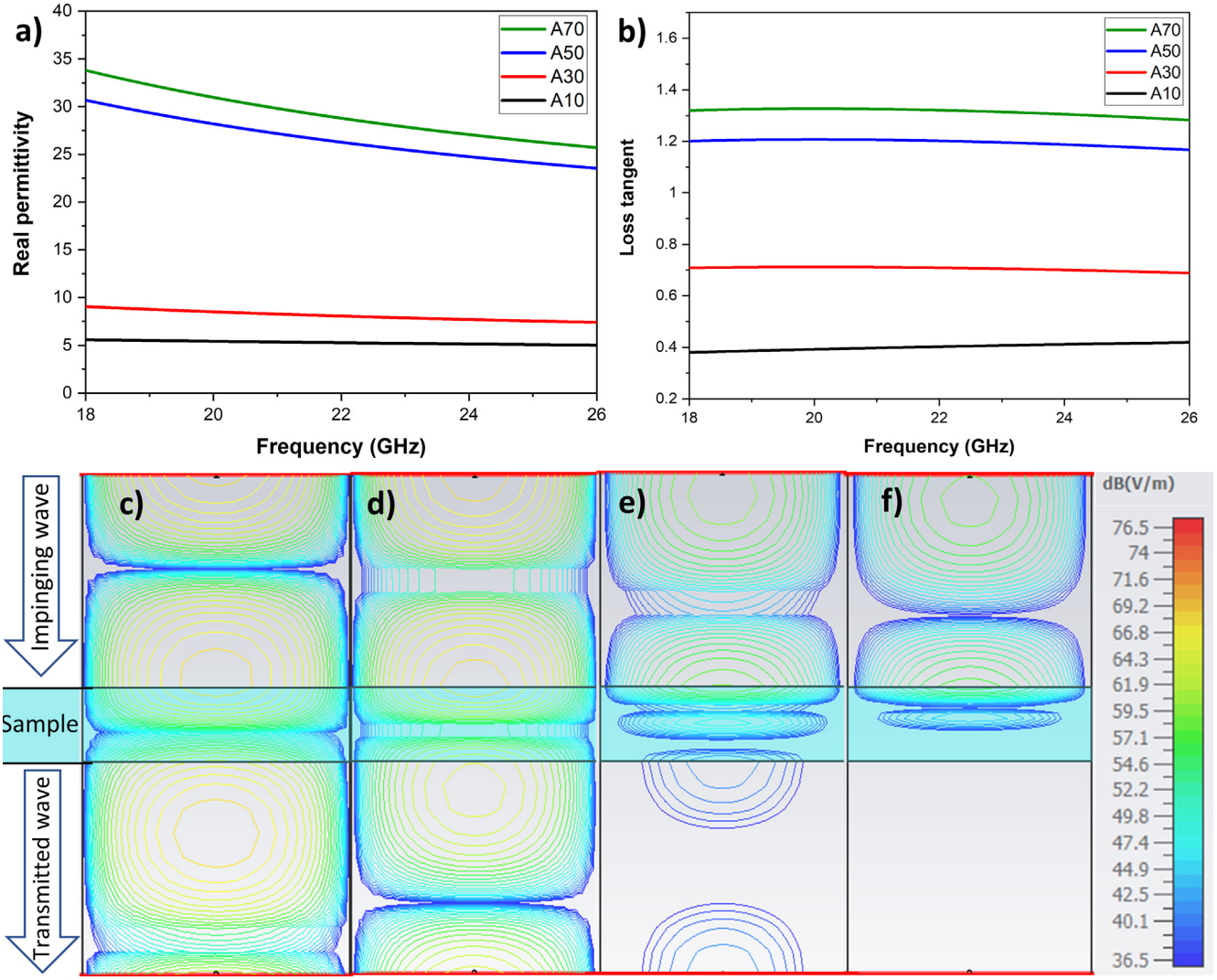

Fig. 8. (a) Real permittivity and (b) Loss tangent of A70, A50, A30, and A10 based on the simulation model, and simulated electric field strength in a waveguide with (c) B10, (d) A30, (e) A50, (f) A70.

the material, and shorter in samples A50 and A70, because the wavelength is inversely proportional to the square root of the dielectric value. The reduced amplitude can also be seen especially in the A50 and A70 samples, because the loss tangent of the materials is large. Deviation of the scattering parameter measurements are presented in Supporting information (Fig. S10). As calculated from the averages of 12 different measurements, the reflection and transmissions coefficients varied by 1 dB and 2 dB, respectively, and the effect of different sample types or freezing direction could not be distinguished based on these measurements. The overall quality of the samples seemed good as the same variation occurred in all samples.

Compared to the behavior of nanocellulose cryogels reported earlier in the literature, the control of cell and surface structure and composition of cryogels can significantly affect permittivity and EMI shielding performance of nanoporous materials, i.e., cryo- and aerogels. Jiang et al. [52] fabricated hierarchically structured unidirectionally frozen MXene-nanocellulose cryogels using epichlorohydrin as a cross-linker. Their 3.5 mm thick cryogel with 28.8 wt % MXene and density of 390 mg/cm^3 reached real permittivity from 11.63 to 8.88 and tangent loss around 0.3 in a frequency range of 2–18 GHz. In this study, an A-type sample with 30 wt % MXene had a similar performance in permittivity but a remarkably lower density of 11.34 mg/cm^3. This improvement was likely promoted by the delamination of the MXene flakes, as indicated by other publications [43,76]. Zeng et al. [43] manufactured a unidirectionally frozen cryogel from TEMPO-modified CNF and 50 wt % MXene with a density of 4 mg/cm^3, achieving EMI SE around 10 dB at frequency from 8 to 12 GHz. A-type cryogel with 50 wt % MXene manufactured in this work had a greater density (15.85 mg/cm^3) and almost twice greater EMI SE, roughly 24 dB at 12 GHz. However, the sample measured from the side opposite to the T gradient had a similar performance to the cryogel reported by Zeng, alluding that surface structure significantly influenced shielding mechanics. Moreover, when further comparing to D-type samples, the lamellar structure with optimized surface properties had higher attenuation levels than the structures consisting of honeycomb cells which are in accordance with other studies [32]. Wang et al. [77] manufactured dense and bulk composites of CNF-MXene using unidirectional freezing followed by thermal annealing and impregnation with epoxy. Their sample with a slightly higher MXene concentration than A50 had EMI SE of roughly 37 dB at 8–12.5 GHz frequency, slightly higher than the result obtained in this work. However, in the present study sample, D50 had a better performance than the corresponding A-type sam-

ple, indicating that bidirectional freezing and surface design helps optimize the EMI SE of porous cryogels.

4. Conclusions

Temperature gradient freeze-drying was harnessed to create self-standing, anisotropic, and cross-linked hybrid cryogels of cellulose nanofibers, PVA and single-layered $Ti_3C_2T_X$ MXene possessing controlled cell and surface architecture with unidirectional (A- and B-type samples) and two-layered honeycomb (C-type samples), and lamellar (D-type samples) pore designs. The hybrid cryogels had low densities (from 9.3 mg/cm^3 to 27.7 mg/cm^3) and very high porosities (from 98.9 % to 99.4 %) depending on the MXene dosage (10–70 wt %), and they were durable when an external force was applied parallel to the freezing direction. The millimeter wave dielectric permittivity of A-type cryogels increased linearly as a function of MXene concentration. It was anisotropic (relative to thickness direction) as the side of cryogels directly exposed to a cold gradient had systemically a higher permittivity. This anisotropy was caused by the thin and smooth outermost surface layer, which covered a unidirectional open honeycomb core structure. The surface structure of all cryogels dominated signal permittivity, while the influence of inner cell structure had only a minor effect on signal propagation. Moreover, the surface layer could compensate for the effects of higher MXene dosages. The A-type cryogels easily achieved the commercial EMI shielding guideline of 20 dB as samples with 70 and 50 wt % of MXene had average attenuation levels of 52 and 37 dB, respectively, while the reflection remained below 3 dB. The attenuation of the 50 wt % sample could be improved to 46 dB with optimized surface design. Overall, the results show that by controlling the freezing conditions for cryogels, green and efficient EMI shielding materials can be produced.

Author contributions

R.H. synthesized the materials and produced the cryogels, and conducted their analysis together with O.L. The permittivity and EMI shielding efficiency was measured by S.M. H.J. and H.L. supervised the work and participated in planning and conceptualizing of the study. The manuscript draft was written by R.H. and was finalized together with all the co-authors.

Data availability

The raw/processed data required to reproduce these findings is available on request.

Declaration of Competing Interest

The authors declare that they have no known competing financial interests or personal relationships that could have appeared to influence the work reported in this paper.

Acknowledgements

The authors acknowledge the financial support from the European Regional Development Fund/Council of Oulu region (Project: "Towards green electronics: Biobased and sustainable applications for the microelectronics"). This research has also been supported by the Academy of Finland, 6G Flagship program under Grant 346208. We also thank the technical support of the Centre for Material Analysis at the University of Oulu and Jasmiini Tornberg for help with graphics.

Appendix A. Supplementary material

Additional experimental details, including sample images, measurement data graphs, and tables. Supplementary data to this article can be found online at https://doi.org/10.1016/j.matdes.2023.111855.

References

[1] Y. Zhang, M. Qiu, Y. Yu, B. Wen, L. Cheng, A novel polyaniline-coated bagasse fiber composite with core-shell heterostructure provides effective electromagnetic shielding performance, ACS Appl. Mater. Interfaces 9 (2017) 809–818, https://doi.org/10.1021/acsami.6b11989.
[2] T.-W. Lee, S.-E. Lee, Y.G. Jeong, Highly effective electromagnetic interference shielding materials based on silver nanowire/cellulose papers, ACS Appl. Mater. Interfaces 8 (2016) 13123–13132, https://doi.org/10.1021/acsami.6b02218.
[3] S. Geetha, K.K. Satheesh Kumar, C.R.K. Rao, M. Vijayan, D.C. Trivedi, EMI shielding: methods and materials-a review, J. Appl. Polym. Sci. 112 (2009) 2073–2086, https://doi.org/10.1002/app.29812.
[4] V.P. Anju, Chapter 6 - nanocellulose-based composites for EMI shielding applications, in: S. Thomas, Y.B. Pottathara (Eds.), Nanocellulose Based Composites for Electronics, Elsevier, 2021, pp. 125–161, https://doi.org/10.1016/B978-0-12-822350-5.00006-0.
[5] J. Tolvanen, J. Hannu, M. Hietala, K. Kordas, H. Jantunen, Biodegradable multiphase poly(lactic acid)/biochar/graphite composites for electromagnetic interference shielding, Compos. Sci. Technol. 181 (2019), https://doi.org/10.1016/j.compscitech.2019.107704 107704.
[6] V. Dupo, F. Belista, V. de Sagun, N. Bugtai, R. Baldovino, A. Abad, J. Dungao, Electromagnetic shielding to improve EMC of a robotic medical device, AIP Conf. Proc. 2193 (2019), https://doi.org/10.1063/1.5139387 050014.
[7] E. Hosseini, M. Arjmand, U. Sundararaj, K. Karan, Filler-free conducting polymers as a new class of transparent electromagnetic interference shields, ACS Appl. Mater. Interfaces 12 (2020) 28596–28606, https://doi.org/10.1021/acsami.0c03544.
[8] P.F. Stenumgaard, K.C. Wiklundh, An improved method to estimate the impact on digital radio receiver performance of radiated electromagnetic disturbances, IEEE Trans. Electromagn. Compat. 42 (2000) 233–239, https://doi.org/10.1109/15.852418.
[9] F. Shahzad, M. Alhabeb, C.B. Hatter, B. Anasori, S. Man Hong, C.M. Koo, Y. Gogotsi, Electromagnetic interference shielding with 2D transition metal carbides (MXenes), Science 353 (2016) 1137–1140, https://doi.org/10.1126/science.aag2421.
[10] W. Zhang, L. Wei, Z. Ma, Q. Fan, J. Ma, Advances in waterborne polymer/carbon material composites for electromagnetic interference shielding, Carbon 177 (2021) 412–426, https://doi.org/10.1016/j.carbon.2021.02.093.
[11] H. Chen, W. Ma, Z. Huang, Y. Zhang, Y. Huang, Y. Chen, Graphene-based materials toward microwave and terahertz absorbing stealth technologies, Adv. Opt. Mater. 7 (2019) 1801318, https://doi.org/10.1002/adom.201801318.
[12] A.K. Singh, A. Shishkin, T. Koppel, N. Gupta, A review of porous lightweight composite materials for electromagnetic interference shielding, Compos. B: Eng. 149 (2018) 188–197, https://doi.org/10.1016/j.compositesb.2018.05.027.
[13] J. Liu, H.-B. Zhang, R. Sun, Y. Liu, Z. Liu, A. Zhou, Z.-Z. Yu, Hydrophobic, flexible, and lightweight MXene foams for high-performance electromagnetic-interference shielding, Adv. Mater. 29 (2017) 1702367, https://doi.org/10.1002/adma.201702367.
[14] X. Li, M. Sheng, S. Gong, H. Wu, X. Chen, X. Lu, J. Qu, Flexible and multifunctional phase change composites featuring high-efficiency electromagnetic interference shielding and thermal management for use in electronic devices, Chem. Eng. J. 430 (2022), https://doi.org/10.1016/j.cej.2021.132928 132928.
[15] S. Zhu, Q. Zhou, M. Wang, J. Dale, Z. Qiang, Y. Fan, M. Zhu, C. Ye, Modulating electromagnetic interference shielding performance of ultra-lightweight composite foams through shape memory function, Compos. B: Eng. 204 (2021), https://doi.org/10.1016/j.compositesb.2020.108497 108497.
[16] J.M. Kim, Y. Lee, M.G. Jang, C. Han, W.N. Kim, Electrical conductivity and EMI shielding effectiveness of polyurethane foam–conductive filler composites, J. Appl. Polym. Sci. 134 (2017), https://doi.org/10.1002/app.44373.
[17] N. Duan, Z. Shi, Z. Wang, B. Zou, C. Zhang, J. Wang, J. Xi, X. Zhang, X. Zhang, G. Wang, Mechanically robust Ti3C2Tx MXene/Carbon fiber fabric/Thermoplastic polyurethane composite for efficient electromagnetic interference shielding applications, Mater. Des. 214 (2022), https://doi.org/10.1016/j.matdes.2022.110382 110382.
[18] H.-G. Shi, H.-B. Zhao, B.-W. Liu, Y.-Z. Wang, Multifunctional flame-retardant melamine-based hybrid foam for infrared stealth, thermal insulation, and electromagnetic interference shielding, ACS Appl. Mater. Interfaces 13 (2021) 26505–26514, https://doi.org/10.1021/acsami.1c07363.
[19] W. Yuan, H. Liu, X. Wang, L. Huang, F. Yin, Y. Yuan, Conductive MXene/melamine sponge combined with 3D printing resin base prepared as an electromagnetic interferences shielding switch, Compos. A: Appl. Sci. Manuf. 143 (2021), https://doi.org/10.1016/j.compositesa.2020.106238 106238.
[20] T. Guo, X. Chen, L. Su, C. Li, X. Huang, X.-Z. Tang, Stretched graphene nanosheets formed the "obstacle walls" in melamine sponge towards effective

electromagnetic interference shielding applications, Mater. Des. 182 (2019), https://doi.org/10.1016/j.matdes.2019.108029 108029.
[21] C. Gao, Y. Shi, Y. Chen, S. Zhu, Y. Feng, Y. Lv, F. Yang, M. Liu, W. Shui, Constructing segregated polystyrene composites for excellent fire resistance and electromagnetic wave shielding, J. Colloid Interface Sci. 606 (2022) 1193–1204, https://doi.org/10.1016/j.jcis.2021.08.091.
[22] M. Aghvami-Panah, A.o. Wang, M. Panahi-Sarmad, S.A.S. Esfahani, A.A. Seraji, M. Shahbazi, R. Ghaffarian, S. Jamalpour, X. Xiao, A comparison study on polymeric nanocomposite foams with various carbon nanoparticles: adjusting radiation time and effect on electrical behavior and microcellular structure, Int. J. Smart Nano Mater. 13 (3) (2022) 504–528, https://doi.org/10.1080/19475411.2022.2107110.
[23] J. Chen, X. Liao, W. Xiao, J. Yang, Q. Jiang, G. Li, Facile and green method to structure ultralow-threshold and lightweight polystyrene/MWCNT composites with segregated conductive networks for efficient electromagnetic interference shielding, ACS Sustain. Chem. Eng. 7 (2019) 9904–9915, https://doi.org/10.1021/acssuschemeng.9b00678.
[24] Z. Zhou, J. Liu, X. Zhang, D. Tian, Z. Zhan, C. Lu, Ultrathin MXene/calcium alginate aerogel film for high-performance electromagnetic interference shielding, Adv. Mater. Interfaces 6 (2019) 1802040, https://doi.org/10.1002/admi.201802040.
[25] M. Yang, Y. Yuan, Y. Li, X. Sun, S. Wang, L. Liang, Y. Ning, J. Li, W. Yin, Y. Li, Anisotropic electromagnetic absorption of aligned Ti3C2Tx MXene/gelatin nanocomposite aerogels, ACS Appl. Mater. Interfaces 12 (2020) 33128–33138, https://doi.org/10.1021/acsami.0c09726.
[26] M.-Z. Li, L.-C. Jia, X.-P. Zhang, D.-X. Yan, Q.-C. Zhang, Z.-M. Li, Robust carbon nanotube foam for efficient electromagnetic interference shielding and microwave absorption, J. Colloid Interface Sci. 530 (2018) 113–119, https://doi.org/10.1016/j.jcis.2018.06.052.
[27] J. Chen, Z. Zhu, H. Zhang, S. Tian, S. Fu, Wood-derived nanostructured hybrid for efficient flame retarding and electromagnetic shielding, Mater. Des. 204 (2021), https://doi.org/10.1016/j.matdes.2021.109695 109695.
[28] H. Qin, Y. Zhang, J. Jiang, L. Wang, M. Song, R. Bi, P. Zhu, F. Jiang, Multifunctional superelastic cellulose nanofibrils aerogel by dual ice-templating assembly, Adv. Funct. Mater. 31 (2021) 2106269, https://doi.org/10.1002/adfm.202106269.
[29] J. Wei, S. Geng, J. Hedlund, K. Oksman, Lightweight, flexible, and multifunctional anisotropic nanocellulose-based aerogels for CO2 adsorption, Cellul. 27 (2020) 2695–2707, https://doi.org/10.1007/s10570-019-02935-7.
[30] A. Tripathi, G.N. Parsons, O.J. Rojas, S.A. Khan, Featherlight, mechanically robust cellulose ester aerogels for environmental remediation, ACS Omega 2 (2017) 4297–4305, https://doi.org/10.1021/acsomega.7b00571.
[31] Z. Wang, L. Song, Y. Wang, X.-F. Zhang, D. Hao, Y. Feng, J. Yao, Lightweight UiO-66/cellulose aerogels constructed through self-crosslinking strategy for adsorption applications, Chem. Eng. J. 371 (2019) 138–144, https://doi.org/10.1016/j.cej.2019.04.022.
[32] Z. Zeng, T. Wu, D. Han, Q. Ren, G. Siqueira, G. Nyström, Ultralight, flexible, and biomimetic nanocellulose/silver nanowire aerogels for electromagnetic interference shielding, ACS Nano 14 (2020) 2927–2938, https://doi.org/10.1021/acsnano.9b07452.
[33] Y. Zhang, W. Tian, L. Liu, W. Cheng, W. Wang, K.M. Liew, B. Wang, Y. Hu, Eco-friendly flame retardant and electromagnetic interference shielding cotton fabrics with multi-layered coatings, Chem. Eng. J. 372 (2019) 1077–1090, https://doi.org/10.1016/j.cej.2019.05.012.
[34] G. Zhu, L. Giraldo Isaza, B. Huang, A. Dufresne, Multifunctional nanocellulose/carbon nanotube composite aerogels for high-efficiency electromagnetic interference shielding, ACS Sustain. Chem. Eng. 10 (2022) 2397–2408, https://doi.org/10.1021/acssuschemeng.1c07148.
[35] H.-D. Huang, C.-Y. Liu, D. Zhou, X. Jiang, G.-J. Zhong, D.-X. Yan, Z.-M. Li, Cellulose composite aerogel for highly efficient electromagnetic interference shielding, J. Mater. Chem. A 3 (2015) 4983–4991, https://doi.org/10.1039/C4TA05998K.
[36] Y.-J. Wan, P.-L. Zhu, S.-H. Yu, R. Sun, C.-P. Wong, W.-H. Liao, Ultralight, super-elastic and volume-preserving cellulose fiber/graphene aerogel for high-performance electromagnetic interference shielding, Carbon 115 (2017) 629–639, https://doi.org/10.1016/j.carbon.2017.01.054.
[37] X. Li, Y. Qu, X. Wang, H. Bian, W. Wu, H. Dai, Flexible graphene/silver nanoparticles/aluminum film paper for high-performance electromagnetic interference shielding, Mater. Des. 213 (2022), https://doi.org/10.1016/j.matdes.2021.110296 110296.
[38] P. Song, B. Liu, H. Qiu, X. Shi, D. Cao, J. Gu, MXenes for polymer matrix electromagnetic interference shielding composites: a review, Compos. Commun. 24 (2021), https://doi.org/10.1016/j.coco.2021.100653 100653.
[39] Y. Zhang, K. Ruan, K. Zhou, J. Gu, Controlled distributed Ti3C2Tx hollow microspheres on thermally conductive polyimide composite films for excellent electromagnetic interference shielding, Adv. Mater. n/a (n.d.) 2211642, doi: 10.1002/adma.202211642.
[40] P. Saravanan, S. Rajeswari, J.A. Kumar, M. Rajasimman, N. Rajamohan, Bibliometric analysis and recent trends on MXene research – a comprehensive review, Chemosphere 286 (2022), https://doi.org/10.1016/j.chemosphere.2021.131873 131873.
[41] M. Malaki, A. Maleki, R.S. Varma, MXenes and ultrasonication, J. Mater. Chem. A 7 (2019) 10843–10857, https://doi.org/10.1039/C9TA01850F.
[42] Y. Gogotsi, B. Anasori, The rise of MXenes, ACS Nano 13 (2019) 8491–8494, https://doi.org/10.1021/acsnano.9b06394.
[43] Z. Zeng, C. Wang, G. Siqueira, D. Han, A. Huch, S. Abdolhosseinzadeh, J. Heier, F. Nüesch, C. Zhang, G. Nyström, Nanocellulose-MXene biomimetic aerogels with orientation-tunable electromagnetic interference shielding performance, Adv. Sci. 7 (15) (2020) 2000979, https://doi.org/10.1002/advs.202000979.
[44] M.-A. Shahbazi, M. Ghalkhani, H. Maleki, Directional freeze-casting: a bioinspired method to assemble multifunctional aligned porous structures for advanced applications, Adv. Eng. Mater. 22 (2020) 2000033, https://doi.org/10.1002/adem.202000033.
[45] M. Zhang, M. Li, Q. Xu, W. Jiang, M. Hou, L. Guo, N. Wang, Y. Zhao, L. Liu, Nanocellulose-based aerogels with devisable structure and tunable properties via ice-template induced self-assembly, Ind. Crop. Prod. 179 (2022), https://doi.org/10.1016/j.indcrop.2022.114701 114701.
[46] W. Gao, N. Zhao, T. Yu, J. Xi, A. Mao, M. Yuan, H. Bai, C. Gao, High-efficiency electromagnetic interference shielding realized in nacre-mimetic graphene/polymer composite with extremely low graphene loading, Carbon 157 (2020) 570–577, https://doi.org/10.1016/j.carbon.2019.10.051.
[47] M. Han, X. Yin, K. Hantanasirisakul, X. Li, A. Iqbal, C.B. Hatter, B. Anasori, C.M. Koo, T. Torita, Y. Soda, L. Zhang, L. Cheng, Y. Gogotsi, Anisotropic MXene aerogels with a mechanically tunable ratio of electromagnetic wave reflection to absorption, Adv. Opt. Mater. 7 (2019) 1900267, https://doi.org/10.1002/adom.201900267.
[48] P. Sambyal, A. Iqbal, J. Hong, H. Kim, M.-K. Kim, S.M. Hong, M. Han, Y. Gogotsi, C.M. Koo, Ultralight and mechanically robust Ti3C2Tx hybrid aerogel reinforced by carbon nanotubes for electromagnetic interference shielding, ACS Appl. Mater. Interfaces 11 (2019) 38046–38054, https://doi.org/10.1021/acsami.9b12550.
[49] T.-B. Ma, H. Ma, K.-P. Ruan, X.-T. Shi, H. Qiu, S.-Y. Gao, J.-W. Gu, Thermally conductive poly(lactic acid) composites with superior electromagnetic shielding performances via 3D printing technology, Chin. J. Polym. Sci. 40 (2022) 248–255, https://doi.org/10.1007/s10118-022-2673-9.
[50] Y. Zhang, Z. Ma, K. Ruan, J. Gu, Multifunctional Ti3C2Tx-(Fe3O4/polyimide) composite films with Janus structure for outstanding electromagnetic interference shielding and superior visual thermal management, Nano Res. 15 (2022) 5601–5609, https://doi.org/10.1007/s12274-022-4358-7.
[51] Y. Guo, H. Qiu, K. Ruan, Y. Zhang, J. Gu, Hierarchically multifunctional polyimide composite films with strongly enhanced thermal conductivity, Nano-Micro Lett. 14 (2021) 26, https://doi.org/10.1007/s40820-021-00767-4.
[52] Y. Jiang, X. Xie, Y. Chen, Y. Liu, R. Yang, G. Sui, Hierarchically structured cellulose aerogels with interconnected MXene networks and their enhanced microwave absorption properties, J. Mater. Chem. C 6 (2018) 8679–8687, https://doi.org/10.1039/C8TC02900H.
[53] Z. Yu, T. Dai, S. Yuan, H. Zou, P. Liu, Electromagnetic interference shielding performance of anisotropic polyimide/graphene composite aerogels, ACS Appl. Mater. Interfaces 12 (2020) 30990–31001, https://doi.org/10.1021/acsami.0c07122.
[54] O. Laitinen, T. Suopajärvi, H. Liimatainen, Enhancing packaging board properties using micro- and nanofibers prepared from recycled board, Cellul. 27 (2020) 7215–7225, https://doi.org/10.1007/s10570-020-03264-w.
[55] M. Alhabeb, K. Maleski, B. Anasori, P. Lelyukh, L. Clark, S. Sin, Y. Gogotsi, Guidelines for synthesis and processing of two-dimensional titanium carbide (Ti3C2Tx MXene), Chem. Mater. 29 (2017) 7633–7644, https://doi.org/10.1021/acs.chemmater.7b02847.
[56] O. Pitkänen, J. Tolvanen, I. Szenti, Á. Kukovecz, J. Hannu, H. Jantunen, K. Kordas, Lightweight hierarchical carbon nanocomposites with highly efficient and tunable electromagnetic interference shielding properties, ACS Appl. Mater. Interfaces 11 (2019) 19331–19338, https://doi.org/10.1021/acsami.9b02309.
[57] M. Shekhirev, C.E. Shuck, A. Sarycheva, Y. Gogotsi, Characterization of MXenes at every step, from their precursors to single flakes and assembled films, Prog. Mater Sci. 120 (2021), https://doi.org/10.1016/j.pmatsci.2020.100757 100757.
[58] B. Anasori, Y. Xie, M. Beidaghi, J. Lu, B.C. Hosler, L. Hultman, P.R.C. Kent, Y. Gogotsi, M.W. Barsoum, Two-dimensional, ordered, double transition metals carbides (MXenes), ACS Nano 9 (2015) 9507–9516, https://doi.org/10.1021/acsnano.5b03591.
[59] G. Akhlamadi, E.K. Goharshadi, H. Liimatainen, Ultrahigh fluid sorption capacity of superhydrophobic and tough cryogels of cross-linked cellulose nanofibers, cellulose nanocrystals, and Ti3C2Tx MXene nanosheets, J. Mater. Chem. A 10 (46) (2022) 24746–24760, https://doi.org/10.1039/D2TA06437E.
[60] X. Zhou, Q. Fu, H. Liu, H. Gu, Z. Guo, Solvent-free nanoalumina loaded nanocellulose aerogel for efficient oil and organic solvent adsorption, J. Colloid Interface Sci. 581 (2021) 299–306, https://doi.org/10.1016/j.jcis.2020.07.099.
[61] P.B. de Oliveira, M. Godinho, A.J. Zattera, Oils sorption on hydrophobic nanocellulose aerogel obtained from the wood furniture industry waste, Cellul. 25 (2018) 3105–3119, https://doi.org/10.1007/s10570-018-1781-8.
[62] J.Y. Seo, Y. Song, J.-H. Lee, H. Kim, S. Cho, K.-Y. Baek, Robust nanocellulose/metal–organic framework aerogel composites: superior performance for static and continuous disposal of chemical warfare agent simulants, ACS Appl. Mater. Interfaces 13 (2021) 33516–33523, https://doi.org/10.1021/acsami.1c08138.
[63] P. Gupta, B. Singh, A.K. Agrawal, P.K. Maji, Low density and high strength nanofibrillated cellulose aerogel for thermal insulation application, Mater. Des. 158 (2018) 224–236, https://doi.org/10.1016/j.matdes.2018.08.031.
[64] X. Zhang, X. Zhao, T. Xue, F. Yang, W. Fan, T. Liu, Bidirectional anisotropic polyimide/bacterial cellulose aerogels by freeze-drying for super-thermal insulation, Chem. Eng. J. 385 (2020), https://doi.org/10.1016/j.cej.2019.123963 123963.

[65] X. Dong, B.W. Chua, T. Li, W. Zhai, Multi-directional freeze casting of porous ceramics with bone-inspired microstructure, Mater. Des. 224 (2022), https://doi.org/10.1016/j.matdes.2022.111344 111344.
[66] J. Chen, B. Shen, X. Jia, Y. Liu, W. Zheng, Lightweight and compressible anisotropic honeycomb-like graphene composites for highly tunable electromagnetic shielding with multiple functions, Mater. Today Phys. 24 (2022), https://doi.org/10.1016/j.mtphys.2022.100695 100695.
[67] B.-W. Liu, M. Cao, Y.-Y. Zhang, Y.-Z. Wang, H.-B. Zhao, Multifunctional protective aerogel with superelasticity over −196 to 500 °C, Nano Res. 15 (2022) 7797–7805, https://doi.org/10.1007/s12274-022-4699-2.
[68] M. Peng, F. Qin, Clarification of basic concepts for electromagnetic interference shielding effectiveness, J. Appl. Phys. 130 (22) (2021) 225108, https://doi.org/10.1063/5.0075019.
[69] Z. Barani, F. Kargar, K. Godziszewski, A. Rehman, Y. Yashchyshyn, S. Rumyantsev, G. Cywiński, W. Knap, A.A. Balandin, Graphene epoxy-based composites as efficient electromagnetic absorbers in the extremely high-frequency band, ACS Appl. Mater. Interfaces 12 (2020) 28635–28644, https://doi.org/10.1021/acsami.0c06729.
[70] M. Zhang, C. Han, W.-Q. Cao, M.-S. Cao, H.-J. Yang, J. Yuan, A nano-micro engineering nanofiber for electromagnetic absorber, green shielding and sensor, Nano-Micro Lett. 13 (2021) 27, https://doi.org/10.1007/s40820-020-00552-9.
[71] J.-M. Thomassin, C. Jérôme, T. Pardoen, C. Bailly, I. Huynen, C. Detrembleur, Polymer/carbon based composites as electromagnetic interference (EMI) shielding materials, Mater. Sci. Eng. R. Rep. 74 (2013) 211–232, https://doi.org/10.1016/j.mser.2013.06.001.
[72] B. Sun, S. Sun, P. He, H.-Y. Mi, B. Dong, C. Liu, C. Shen, Asymmetric layered structural design with segregated conductive network for absorption-dominated high-performance electromagnetic interference shielding, Chem. Eng. J. 416 (2021), https://doi.org/10.1016/j.cej.2021.129083 129083.
[73] L. Xu, L. Wang, W. Zhang, J. Xue, S. Hou, The reinforced electromagnetic interference shielding performance of thermal reduced graphene oxide films via polyimide pyrolysis, ACS Omega 7 (2022) 10955–10962, https://doi.org/10.1021/acsomega.1c06767.
[74] H. Xu, X. Yin, X. Li, M. Li, S. Liang, L. Zhang, L. Cheng, Lightweight Ti2CTx MXene/poly(vinyl alcohol) composite foams for electromagnetic wave shielding with absorption-dominated feature, ACS Appl. Mater. Interfaces 11 (2019) 10198–10207, https://doi.org/10.1021/acsami.8b21671.
[75] A. Prokopchuk, I. Zozulia, Y. Didenko, D. Tatarchuk, H. Heuer, Y. Poplavko, Dielectric permittivity model for polymer-filler composite materials by the example of Ni- and graphite-filled composites for high-frequency absorbing coatings, Coatings 11 (2021) 172, https://doi.org/10.3390/coatings11020172.
[76] Y. Li, Y. Chen, X. He, Z. Xiang, T. Heinze, H. Qi, Lignocellulose nanofibril/gelatin/MXene composite aerogel with fire-warning properties for enhanced electromagnetic interference shielding performance, Chem. Eng. J. 431 (2021), https://doi.org/10.1016/j.cej.2021.133907 133907.
[77] L. Wang, P. Song, C.-T. Lin, J. Kong, J. Gu, 3D Shapeable, superior electrically conductive cellulose nanofibers/Ti3C2Tx MXene aerogels/epoxy nanocomposites for promising EMI shielding, Research 2020 (2020) 4093732, https://doi.org/10.34133/2020/4093732.